PHOTONICS Research

Amplification assisted difference frequency generation for efficient mid-infrared conversion based on monolithic tandem lithium niobate superlattice

TAO CHEN, HAO LIU, WEI KONG, AND RONG SHU*

Key Laboratory of Space Active Opto-Electronics Technology, Shanghai Institute of Technical Physics, Chinese Academy of Sciences, Shanghai 200083, China

**Corresponding author: shurong@mail.sitp.ac.cn*

Received 15 February 2017; revised 4 May 2017; accepted 5 May 2017; posted 9 May 2017 (Doc. ID 286845); published 13 July 2017

We report the investigation on the performance of an amplification assisted difference frequency generation (AA-DFG) system driven by pulsed pump and continuous-wave primary signal lasers. A monolithic tandem lithium niobate superlattice was employed as the nonlinear crystal with a uniform grating section for the DFG process, followed by a chirp section for the optical parametric amplification process. The impacts of pump pulse shape, primary signal power, input beam diameter, and crystal structure on the pump-to-idler conversion efficiency of the AA-DFG system were comprehensively studied by numerically solving the coupled wave equations. It is concluded that square pump pulse and high primary signal power are beneficial to high pump-to-idler conversion efficiency. In addition, tighter input beam focus and smaller DFG length proportion could redeem the reduction in conversion efficiency resulting from wider acceptance bandwidths for the input lasers. We believe that such systems combining the merits of high stability inherited from cavity-free configuration and high efficiency attributed from the cascaded nonlinear conversion should be of great interest to a wide community, especially when the pulse shaping technique is incorporated. © 2017 Chinese Laser Press

OCIS codes: (190.4970) Parametric oscillators and amplifiers; (190.4410) Nonlinear optics, parametric processes; (140.3070) Infrared and far-infrared lasers.

https://doi.org/10.1364/PRJ.5.000355

1. INTRODUCTION

To date, mid-infrared (MIR) lasers have become the workhorses for scientific research, environmental monitoring, and defense systems, enabling high-resolution operation in the temporal, spectral, and spatial domains [1–3]. Among all the MIR generation methods, the optical parametric oscillator (OPO) stands out from its counterparts due to its broad operating temperature, wide wavelength tuning range, and high power scalability. Since its advent, this method has been extensively adopted to generate MIR radiation with output durations from continuous wave (CW) to femtosecond [4–10]. However, the pump-to-idler conversion efficiency of a conversional OPO is intrinsically restricted by the Manley–Rowe relations, in which the generation of any demanded MIR idler photons is always accompanied by the same amount of unwanted near-infrared signal photons. In addition, the inefficient parametric conversion during the buildup phase and probable parametric back-conversion during oscillation will further reduce the actual pump-to-idler conversion efficiency in practice.

To tackle this crisis, the scheme of the cascaded OPO (COPO) was proposed, in which the generated intracavity signal photons were recycled partly to produce the idler photons once more via a secondary optical parametric amplification (OPA) process [11]. Thanks to the prosperity of quasi-phase-matching technology, COPOs harnessed by monolithic aperiodically poled or tandem structured ferroelectric crystals have been demonstrated theoretically and/or experimentally, in either nanosecond [12–18] or picosecond [19] regime. Nevertheless, inevitable drawbacks inherited from the oscillating cavity remained for both OPOs and COPOs, including complicated coating, susceptibility to misalignment, mode hopping, and thermal induced instability. Especially when pumped by lasers with high repetition rate and high average power, the thermal bistable behavior of such OPOs or COPOs may hinder them from operating in pulse-on-demand mode [20], which happens to be one of the favorite operation modes for biomedical research or MIR countermeasures.

As an alternative, amplification assisted difference frequency generation (AA-DFG) featuring cavity-free configuration can

intrinsically avoid the flaws incurred by the resonant cavity, while the OPA stage can still improve the pump-to-idler conversion efficiency to some extent [21]. However, in the early trials, several nonlinear crystals were aligned successively to produce efficiency-enhanced MIR radiation. Although the phase-matching conditions for each nonlinear process could be optimized independently, separated crystals would ineluctably increase the loss and dimensions, thereby deteriorating the conversion efficiency as well as the long-term stability. This shortcoming was then resolved by Figen, introducing an aperiodically poled MgO-doped lithium niobate (APMgLN) crystal to phase match the two parametric conversion processes simultaneously [22]. Nevertheless, only Gaussian-shaped pump pulse and low-power primary signal lasers were considered in his model. More importantly, when such APMgLN crystals were adopted in AA-DFG systems, the pump and signal wavelengths as well as the crystal temperature should be precisely matched, and therefore the output MIR radiation was also wavelength fixed. This would inevitably bring difficulties to the construction of an AA-DFG system and reduce its wavelength adaptability. One possible solution to this issue is to utilize a tandem lithium niobate (LN) superlattice with a uniform grating section for the primary DFG process followed by a fan-out grating section for the succeeding OPA process [23]. In this scenario, the additional freedom in OPA's domain periodicity could alleviate the strict simultaneous phase-matching condition. Slight wavelength deviation of the input lasers could be compensated by laterally moving the crystal position and tuning the crystal temperature accordingly. However, the movable components might still prevent such systems from operating in a harsh environment. Another possible method is to introduce a certain chirp rate to the secondary OPA process so as to broaden the acceptance bandwidths of the input lasers. Although this structure has been employed to generate MIR in COPO configuration [24], it has yet to be adopted in an AA-DFG system. In addition, considering that pulse-shaped fiber lasers [25] and widely tunable high-power Raman fiber lasers (RFLs) [26] are readily available for the time being, comprehensive studies on the impacts of the pump pulse shape, primary signal power, input beam diameter, and crystal structure on the performance of a tandem LN superlattice-based AA-DFG system are in great demand.

Herein we report our numerical investigations on the AA-DFG system based on a multichannel tandem LN superlattice driven by pulsed pump and CW primary signal lasers. Each channel of the LN superlattice was designed with a uniform section for the DFG process followed by a chirped section for the OPA process so as to enhance the conversion efficiency by the OPA process and broaden the acceptance bandwidths for the input lasers with the chirp design. The chirp design could also offer possibilities of idler wavelength tuning as long as the pump and/or primary signal were wavelength tunable. The optimal working conditions in terms of the highest pump-to-idler conversion efficiency were obtained by numerically computing the coupled wave equations. Two kinds of pump pulse shapes, namely, Gaussian and square shapes with identical peak power, and primary signal with different average powers were considered in the calculation. The results indicated that square pump pulses and higher primary signal power were beneficial to higher idler generation rate. Later calculations were focused on the optimization of beam diameter and crystal structure for square pulse pumped AA-DFG systems with either 0.4 or 4 W primary signal powers, which were typical values for semiconductor lasers or RFLs, respectively. It is concluded that tighter beam focus and smaller DFG length proportion can redeem the deterioration in conversion efficiency resulting from wider acceptance bandwidths for the input lasers. In addition, for AA-DFG systems with lower primary signal power, even tighter beam focus should be adopted to get the most efficient MIR conversion, though their optimal conversion efficiencies were slightly inferior to those with higher primary signal powers. In spite of this, the AA-DFG system with low primary signal power still exceeds the single DFG system in conversion efficiency under the same pump conditions. We believe that such systems combining the merits of high stability inherited from cavity-free configuration and high efficiency attributed from the cascaded nonlinear conversion are of great interest to researchers in this realm, especially when the advanced pulse shaping and RFL technology are incorporated.

2. MODEL AND SIMULATION

The schematic diagram of the tandem LN superlattice-based AA-DFG system is depicted in Fig. 1. The pump and primary signal lasers were combined with the help of a dichroic mirror enabling independent beam focusing for good mode overlap. The pump laser was supposed to be a pulsed fiber laser producing either Gaussian or square pulses with identical peak power of 20 kW at 1.065 μm, which is typical for a linearly polarized, Yb-doped fiber laser incorporating pulse shaping [27]. There were two kinds of CW primary signal lasers considered in our model, namely, the fiber pigtailed semiconductor laser and RFL, covering the power range from several milliwatts up to 4 W around the 1.48 μm band [26] for different financial budgets. The calculated idler wavelength was therefore at the ~3.8 μm band. The primary signal laser was operated in CW mode rather than pulsed mode so that it could adapt to most possible operation modes of the pump laser, including the versatile pulse-on-demand mode, without synchronization or pulse width adjustment.

The nonlinear crystal was a 50 mm long monolithic multichannel LN superlattice designed in tandem structure, where the former and latter grating sections satisfied the phase-matching conditions of the DFG and OPA processes, respectively. In particular, the latter grating section for the OPA process was slightly chirped with different rates so as to broaden the pump and/or

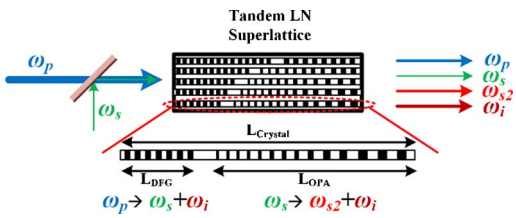

Fig. 1. Scheme of the AA-DFG system based on a monolithic multichannel tandem LN superlattice.

primary signal acceptance bandwidths to different extents. The merits of such a design are twofold. First of all, this would relieve the strict wavelength requirement for the pump and primary signal, which could reduce their fabrication difficulties. In addition, if the pump and/or primary signal lasers were slightly tunable, such a design could also provide certain idler wavelength tunability, which would be indispensable to remote sensing or biomedical applications [2].

To optimize the crystal design as well as the beam diameter under different pump and primary signal input conditions, the amplitudes of the four major interacting waves propagating along the nonlinear crystal, namely, the pump, the primary signal, the secondary signal, and the idler, should be calculated by numerically solving the coupled wave equations. The nonlinear conversion starts with the DFG process in the first section of the LN superlattice, where the idler is produced and the primary signal also gets amplified from pump depletion. Afterward, the amplified primary signal continues to boost the amplitude of the idler accompanied with the generation of the secondary signal in the following OPA section. Thanks to the simple single pass scheme and independent interacting structures, the two nonlinear processes can be solved successively using the following coupled wave equations [Eqs. (1)–(3) for DFG and Eqs. (4)–(6) for OPA]:

$$\frac{dA_p}{dz} = -\frac{\alpha_p}{2}A_p - \frac{1}{2ik_p}\left(\frac{\partial}{\partial x^2} + \frac{\partial}{\partial y^2}\right)A_p + \kappa_{\mathrm{DFG},p}A_sA_ie^{-i\Delta k_{\mathrm{DFG}}Z}, \tag{1}$$

$$\frac{dA_s}{dz} = -\frac{\alpha_s}{2}A_s - \frac{1}{2ik_s}\left(\frac{\partial}{\partial x^2} + \frac{\partial}{\partial y^2}\right)A_s + \kappa_{\mathrm{DFG},s}A_pA_i^*e^{i\Delta k_{\mathrm{DFG}}Z}, \tag{2}$$

$$\frac{dA_i}{dz} = -\frac{\alpha_i}{2}A_i - \frac{1}{2ik_i}\left(\frac{\partial}{\partial x^2} + \frac{\partial}{\partial y^2}\right)A_i + \kappa_{\mathrm{DFG},i}A_pA_s^*e^{i\Delta k_{\mathrm{DFG}}Z}, \tag{3}$$

$$\frac{dA_s}{dz} = -\frac{\alpha_s}{2}A_s - \frac{1}{2ik_s}\left(\frac{\partial}{\partial x^2} + \frac{\partial}{\partial y^2}\right)A_s + \kappa_{\mathrm{OPA},s}A_{s2}A_ie^{-i\Delta k_{\mathrm{OPA}}Z}, \tag{4}$$

$$\frac{dA_{s2}}{dz} = -\frac{\alpha_{s2}}{2}A_{s2} - \frac{1}{2ik_{s2}}\left(\frac{\partial}{\partial x^2} + \frac{\partial}{\partial y^2}\right)A_{s2} + \kappa_{\mathrm{OPA},s2}A_sA_i^*e^{i\Delta k_{\mathrm{OPA}}Z}, \tag{5}$$

$$\frac{dA_i}{dz} = -\frac{\alpha_i}{2}A_i - \frac{1}{2ik_i}\left(\frac{\partial}{\partial x^2} + \frac{\partial}{\partial y^2}\right)A_i + \kappa_{\mathrm{OPA},i}A_sA_{s2}^*e^{i\Delta k_{\mathrm{OPA}}Z}, \tag{6}$$

where $\Delta k_{\mathrm{DFG}} = k_p - k_s - k_i$ and $\Delta k_{\mathrm{OPA}} = k_s - k_{s2} - k_i$ are the phase mismatches for the DFG and OPA processes, respectively. $\kappa_{\mathrm{DFG},j} = i\omega_j d_{\mathrm{DFG}}g(z)/(cn_j)$ and $\kappa_{\mathrm{OPA},j} = i\omega_j d_{\mathrm{OPA}}g(z)/(cn_j)$ are the coupling coefficients for wave j in the DFG and OPA processes, respectively. $g(z)$ is the modulation function of the nonlinear coefficient χ^2 related to the domain structure of the LN superlattice. $d_{\mathrm{DFG}} = 1/2\,\chi^2_{\mathrm{DFG}}$ and $d_{\mathrm{OPA}} = 1/2\chi^2_{\mathrm{OPA}}$ are the nonlinear coefficients for the DFG and OPA processes, respectively. c is the speed of light in vacuum. A, α, n, and ω are the amplitude, attenuation coefficient, reflective index, and angular frequency, respectively. The subscripts p, s, i, and $s2$ denote the pump, the primary signal, the idler, and the secondary signal waves, respectively.

The coupled wave equations were computed according to the algorithm proposed by Drag *et al.* [28], where all the interacting waves were divided spatially and temporally at first. On account of the circular symmetry characteristic of Gaussian beams with fundamental mode, the interacting fields are discretized radially with 128 equally spaced rings in their cross sections. By contrast, the time slices are unevenly divided according to the pump pulse shapes, which was a trade-off between the calculation efficiency and accuracy. The amplitudes of the discretized interacting waves were calculated in parallel using the split-step method, by which the diffraction and propagation terms were alternatively computed. At the exit of the nonlinear crystal, the calculated beam intensities for each wave were integrated in both time and space domain, from which the pump-to-idler conversion efficiency could be obtained to assess the performance of an AA-DFG system for efficiency optimization.

3. RESULTS AND DISCUSSION

To investigate the impact of pump pulse shape as well as the primary signal power on the performance of an AA-DFG system, the pump-to-idler conversion efficiencies for pump pulses with Gaussian and square shapes with 20 kW peak power and 50 ns pulse duration (full width at half-maximum, FWHM) were calculated and are depicted in Figs. 2(a) and 2(b), respectively. The pump and primary signal wavelengths were 1.065 and 1.48 μm, respectively, with calculated domain periodicities of 29.55 and 33.66 μm for the DFG and OPA sections, respectively, when the crystal temperature was 45°C, according to the Sellmeier equation of MgO-doped congruent $LiNbO_3$ crystal [29]. Indeed, optimal working conditions for pump pulses with different shapes were dissimilar even if their pump peak powers and pulse durations were identical. Therefore, variable primary signal powers and DFG length proportion were adopted in the calculation to find the peak pump-to-idler conversion efficiencies for both cases. Meanwhile, the input beam diameters of the two cases were both set to be 360 μm for a better comparison. Figures 2(c) and 2(d) plot the calculated pulse profiles of the four interacting waves at the exit of the nonlinear crystal together with the input pump pulse shapes under the circled working points possessing the highest pump-to-idler conversion efficiency for each case.

It can be concluded from Figs. 2(a) and 2(b) that higher input primary signal power is beneficial to higher pump-to-idler conversion efficiency, peaking at 16.7% and 22.65%, respectively, for Gaussian and square pump pulses. Intense primary signal could not only effectively generate the idler but also rapidly enhance its own intensity from pump depletion in the DFG process, leading to even higher primary signal intensity for the OPA process. And the intensified primary signal

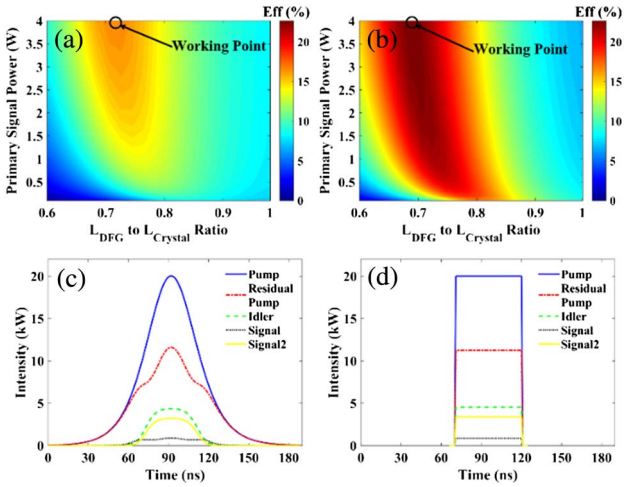

Fig. 2. Performances of the AA-DFG system pumped by Gaussian- or square-shaped pulses with 20 kW peak power and 50 ns duration. (a), (b) Pump-to-idler conversion efficiencies under different primary signal power and DFG length proportion; the color bars show the pump-to-idler conversion efficiency in percentage. (c), (d) Pulse profiles of the pump, residual pump, idler, primary signal, and secondary signal under the circled optimal working points for both cases. (a), (c) Pumped by Gaussian pulses. (b), (d) Pumped by square pulses.

was also advantageous to efficient idler amplification in the OPA process. Consequently, the idler generation is more efficient with higher primary signal power for both cases. However, the highest pump-to-idler conversion efficiency of Gaussian pump pulses was inferior to that of square pump pulses with the same primary signal power, because the efficiency optimization of Gaussian pump pulses was a compromise among different peak powers within the pump duration. The optimal L_{DFG} to L_{Crystal} ratio of ~0.72 is the most suitable only for pump power slightly lower than the peak pump power. Backconversion and inefficient conversion would inevitably take place around the peak and at the vicinity of the leading and trailing edges of the pump pulse, respectively, sacrificing the overall pump-to-idler conversion efficiency, as was implied in Fig. 2(c) (the bump around the peak of the residual pump pulse indicating the backconversion, and negligible idler power at the vicinity of the leading and trailing edges indicating the inefficient conversion). By contrast, the peak power of a square pulse was constant, and therefore only this value should be considered during efficiency optimization. As a result, the most efficient idler production could be realized within the whole pump duration with the most suitable L_{DFG} to L_{Crystal} ratio at ~0.68 leading to higher overall pump-to-idler conversion efficiency, which could also be deduced from Fig. 2(d).

In addition to the pump-to-idler conversion efficiency, the acceptance bandwidths for the input lasers are also crucial in practice. Because of the uncertainty in the applicability of the Sellmeier equation to the LN wafer, the designed crystal structure is usually not perfectly phase matched at the expected wavelengths and crystal temperature. In the COPO scenario, the secondary OPA process may turn into a secondary OPO process, leading to efficiency degradation [12–16]. This uncertainty problem could be solved by tuning the crystal temperature. In this way, the idler wavelengths produced from the OPO and OPA processes would vary with different trends and finally coincide at the working point [12–16]. Different from COPOs, both the pump and primary signal are externally injected and their wavelengths may hardly be tuned when the uncertainty problem occurs. Moreover, the secondary OPA process could never turn into a secondary OPO process and would result in phase mismatch, making the efficiency reduction even more severe. To ease the phase-matching conditions for the two nonlinear processes, certain chirp rates should be induced into the OPA section to broaden the pump and/or primary signal acceptance bandwidths in case of possible input wavelength deviation and/or uncertainty in the Sellmeier equation. Indeed, crystal temperature should also participate in broadening the acceptance bandwidths of the input lasers for such AA-DFG systems. Because the grating for the DFG process is uniform, the wavelength deviation of the input lasers and/or uncertainty in the Sellmeier equation can be made up by changing the crystal temperature. As for the secondary OPA section, as the interacting wavelengths and crystal temperature have all been determined, the only variable remaining to fulfill the phase-matching condition becomes the domain periodicity in this section. When the wavelengths of the input lasers change, the crystal temperature should change first, which is determined by the primary DFG section. Related changes should be made afterward on domain periodicity in the secondary OPA section according to the combination of input wavelengths and crystal temperature drift. Eventually, these changes would form certain working ranges, which are defined as acceptance bandwidth, temperature tuning range, and domain periodicity variation in this paper.

Figure 3 plots the characteristics of the acceptance bandwidths for the pump and primary signal lasers. The central wavelengths of the input lasers and DFG domain periodicity were identical to those in the previous calculations. And the OPA domain periodicity was slightly chirped around the previous value according to the desired acceptance bandwidths. Figure 3(a) shows the OPA domain periodicity variation for different pump and primary signal acceptance bandwidths. Clearly, larger domain periodicity variation should be induced if both input lasers possessed the largest acceptance bandwidths, and this figure reached 0.244 μm if the wavelengths of the two lasers were located at any point within ±5 nm from central wavelengths. The required temperature tuning ranges were calculated and demonstrated in Fig. 3(b), peaking at

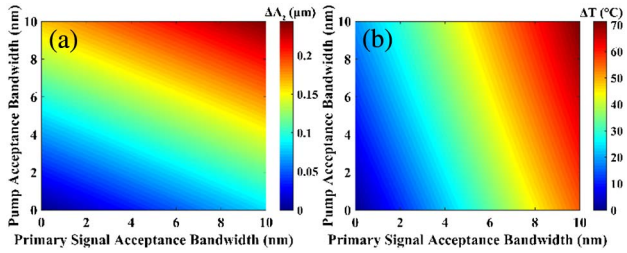

Fig. 3. Acceptance bandwidths of the pump and primary signal laser with respect to (a) OPA domain periodicity variation, and (b) crystal temperature tuning range. The color bars show the periodicity variation in micrometers and temperature tuning range in degrees Celsius.

~70°C for the largest possible wavelength deviation of 10 nm each for the two input lasers.

As the acceptance bandwidths and peak powers of the input lasers are determined, the optimization of an AA-DFG system becomes the coordination between the DFG length proportion of the LN superlattice and the beam diameter of the input lasers. Because there are two kinds of primary signal lasers available, namely, the pigtailed semiconductor laser and the RFL, typical primary signal powers of 0.4 and 4 W at 1.48 μm were selected, respectively, in the following calculation. The pump wavelength and peak power were set to be 1.065 μm and 20 kW with square shape, respectively. The pump-to-idler conversion efficiency with respect to input beam diameter and DFG length proportion for primary signal power of 0.4 W with different OPA domain periodicity variations of 0, 0.06, 0.12, and 0.24 μm are plotted in Figs. 4(a)–4(d), respectively. These values for primary signal power of 4 W are illustrated in Figs. 5(a)–5(d).

The pump-to-idler conversion efficiency of an AA-DFG system with zero OPA chirp peaked at 20.7% for 0.4 W primary signal power, and the corresponding input beam diameter and DFG length proportion were 345 μm and 0.745, respectively. These values were then reduced gradually with the increase of the OPA chirp rate, reaching 20%, 188 μm, and 0.41, respectively, when the OPA's domain periodicity variation was 0.24 μm. The calculated results witnessed similar trends when the input primary signal power was raised by an order of magnitude to 4 W. The peak pump-to-idler conversion efficiency stood at 23.4% as the beam diameter and DFG length proportion were 390 μm and 0.71, respectively, in the scenario of zero chirp rate. These values decreased to 22.6%, 200 μm, and 0.365, respectively, in the case of the largest OPA domain periodicity variation of 0.24 μm.

Despite that the induced chirp in the OPA section would inevitably reduce the effective interacting length and result in lower pump-to-idler conversion efficiency, tighter input beam focus and readjustment of the DFG length ratio could always redeem the performance deterioration of such an AA-DFG system to some extent, as long as the pump density was below the damage threshold of the crystal, and the beam confocal parameter was larger than the crystal length. Therefore, only subtle degradation in pump-to-idler conversion efficiency occurred in both cases even though the wavelength tolerance of the input lasers was increased from almost zero to 10 nm each. It is also worth mentioning that when the DFG length proportion reaches unity, such an AA-DFG system becomes a single-stage DFG system. Under this condition, the highest pump-to-conversion efficiency was only around 12% even if it was pumped by the favorable square pulses with optimal beam diameter. In other words, the AA-DGF scheme could offer an efficiency enhancement of more than 50% compared with the single-stage DFG, even though the largest input wavelength tolerance of 10 nm each and the smaller primary signal power of 0.4 W were selected.

Figure 6 compares the optimal DFG length proportion, beam diameter, and pump-to-idler conversion efficiency with

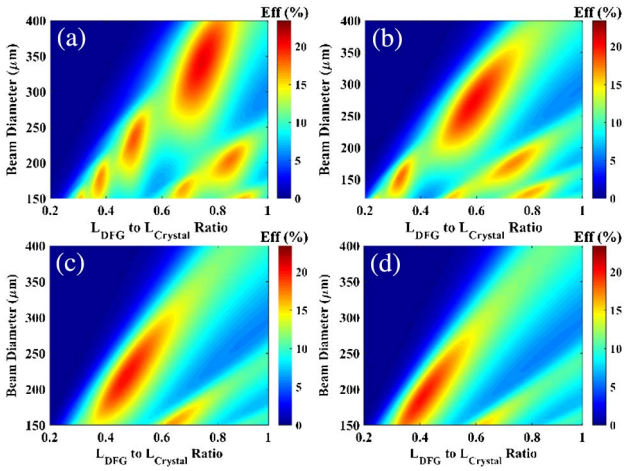

Fig. 4. Pump-to-idler conversion efficiency with respect to input beam diameter and DFG length proportion for primary signal power of 0.4 W with different OPA domain periodicity variations. (a) 0, (b) 0.06, (c) 0.12, and (d) 0.24 μm. The color bars show the pump-to-idler conversion efficiency in percentage.

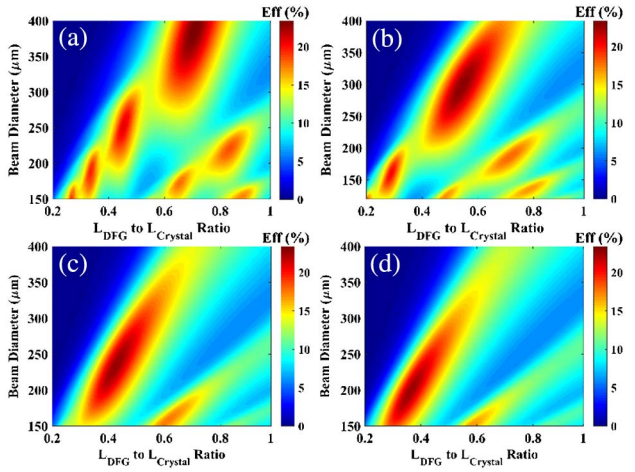

Fig. 5. Pump-to-idler conversion efficiency with respect to input beam diameter and DFG length proportion for primary signal power of 4 W with different OPA domain periodicity variations. (a) 0, (b) 0.06, (c) 0.12, and (d) 0.24 μm. The color bars show the pump-to-idler conversion efficiency in percentage.

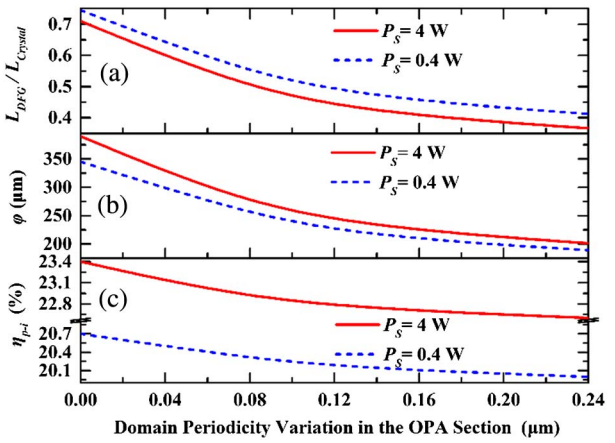

Fig. 6. Comparisons between AA-DFG systems with input primary signal powers of 4 W and 0.4 W on the (a) optimal length proportion of DFG section, (b) input beam diameter, and (c) pump-to-idler conversion efficiency with respect to OPA domain periodicity variation.

respect to the OPA domain periodicity variation for primary signal powers of 4 and 0.4 W. The optimal DFG length proportions for AA-DFG systems with primary signal power of 0.4 W were larger than those for primary signal power of 4 W if they possess the same OPA domain periodicity variation, as shown in Fig. 6(a). The optimal beam diameters for the two cases showed an opposite situation, as was illustrated in Fig. 6(b). Clearly, larger primary signal power would deplete the pump more efficiently, and therefore shorter DFG length and looser focus should be applied to avoid severe backconversion in this section. Fortunately, even with the largest domain periodicity variation and the smaller primary signal power, the tightest pump beam was still 188 μm in diameter with calculated confocal parameter of 112 mm, which is more than 2 times larger than the crystal length. The loose focusing condition could also relieve the risk of crystal damage at the waist of the pump beam. Other than the pump beam, a more intense primary signal could produce idler more efficiently in the DFG process, and meanwhile its own intensity could also grow faster from pump depletion. As a result, higher primary signal intensity could be obtained after the DFG section, leading to higher idler amplification rate in the OPA process. Because idler conversion of both processes could benefit from higher primary signal power, the overall effect would result in much higher pump-to-idler conversion efficiencies under higher primary signal powers, as indicated in Fig. 6(c).

It is also noteworthy that the pump-to-idler conversion efficiency of an AA-DFG system is still inferior to that of a COPO even when the AA-DFG is in its favorable conditions, including the highest primary signal power and square pump pulses, whereas the pump pulse shape for the COPO is only Gaussian [24]. Undoubtedly, the COPO cavity circulating the primary signal could make the best use of its intracavity primary signal power and thus produce idler more effectively than an AA-DFG system. However, the cavity would also bring about an instability issue caused by misalignment and thermal lens effect. Especially when operated in pulse-on-demand mode, a different overall duty cycle will lead to significant differences in thermal conditions, affecting the mode overlap between the oscillating primary signal and pump beams. As a result, the conversion efficiency would vary under different pump repetition rates, even if each pump pulse was identical. Worse, the oscillating cavity might sometimes turn into an unstable resonator under certain thermal conditions, which is disastrous to practical applications. By contrast, good mode overlap can always be realized for an AA-DFG system, providing excellent stability with much better pump-to-conversion efficiency than a single-stage DFG or OPO, which is suitable for generating high-power MIR radiation for countermeasures or biomedical applications.

4. CONCLUSIONS

In summary, we have numerically studied the performance of an AA-DFG system based on multichannel tandem LN superlattice driven with pulsed pump and CW primary signal lasers. It is concluded that square pump pulses and higher primary signal power are beneficial to higher pump-to-idler conversion efficiency. In addition, the DFG length proportion and the beam diameter both play important roles in optimizing the performance of an AA-DFG system with different acceptance bandwidths for the input lasers. Although the optimal pump-to-idler conversion efficiency of such an AA-DFG system is inferior to that of a COPO system, its optimized pump-to-idler conversion efficiency is still much better than a single-stage OPO or DFG system. Moreover, the cavity-free configuration can fully avoid the power instability incurred by the thermal effect and misalignment, thereby improving its performance to a great extent and making it suitable for versatile operation modes, including pulse-on-demand mode. We believe that such an AA-DFG system combining the merits of excellent stability, high pump-to-idler conversion efficiency, and certain acceptance bandwidths has provided a promising solution to the production of high-power MIR radiation for practical applications.

Funding. National Natural Science Foundation of China (NSFC) (61505236); Key Laboratory Foundation of Chinese Academy of Sciences (CAS) (CXJJ-15S099, CXJJ-17S026); Innovation Foundation of Shanghai Institute of Technical Physics (CX-54).

REFERENCES

1. A. Godard, G. Aoust, J. Armougom, E. Cadiou, D. Descloux, G. Walter, J.-B. Dherbecourt, G. Gorju, J.-M. Melkonian, M. Raybaut, and M. Lefebvre, "Optical parametric sources for gas sensing applications," Proc. SPIE **10111**, 101112X (2017).
2. D. D. Arslanov, M. Spunei, J. Mandon, S. M. Cristescu, S. T. Persijn, and F. J. Harren, "Continuous-wave optical parametric oscillator based infrared spectroscopy for sensitive molecular gas sensing," Laser Photon. Rev. **7**, 188–206 (2013).
3. B. Molocher, "Countermeasure laser development," Proc. SPIE **5989**, 598902 (2005).
4. W. Tian, Z. Wang, J. Zhu, and Z. Wei, "Harmonically pumped femtosecond optical parametric oscillator with multi-gigahertz repetition rate," Opt. Express **24**, 29814–29821 (2016).
5. K. Wei, X. Zhou, and X. Lai, "3.8-μm mid-infrared laser quasi-synchronously pumped by a MOPA structured picosecond Yb fiber amplifier with multi-pulse operation," IEEE Photon. J. **8**, 1503905 (2016).
6. T. Chen, H. Liu, Y. Huang, and R. Shu, "High-efficiency PPMgLN-based mid-infrared optical parametric oscillator pumped by a MOPA-structured fiber laser with long pulse duration," Laser Phys. **25**, 125401 (2015).
7. L. Xu, H. Y. Chan, S. U. Alam, D. J. Richardson, and D. P. Shepherd, "Fiber-laser-pumped, high-energy, mid-IR, picosecond optical parametric oscillator with a high-harmonic cavity," Opt. Lett. **40**, 3288–3291 (2015).
8. S. C. Kumar, J. Wei, J. Debray, V. Kemlin, B. Boulanger, H. Ishizuki, T. Taira, and M. Ebrahim-Zadeh, "High-power, widely tunable, room-temperature picosecond optical parametric oscillator based on cylindrical 5% MgO: PPLN," Opt. Lett. **40**, 3897–3900 (2015).
9. P. Wang, Y. Shang, X. Li, M. Shen, and X. Xu, "Multiwavelength mid-infrared laser generation based on optical parametric oscillation and intracavity difference frequency generation," IEEE Photon. J. **9**, 1500107 (2017).
10. Y. Shang, J. Xu, P. Wang, X. Li, P. Zhou, and X. Xu, "Ultra-stable high-power mid-infrared optical parametric oscillator pumped by a superfluorescent fiber source," Opt. Express **24**, 21684–21692 (2016).
11. G. T. Moore and K. Koch, "The tandem optical parametric oscillator," IEEE J. Quantum Electron. **32**, 2085–2094 (1996).
12. G. Porat, O. Gayer, and A. Arie, "Simultaneous parametric oscillation and signal-to-idler conversion for efficient downconversion," Opt. Lett. **35**, 1401–1403 (2010).
13. Y. H. Liu, Z. D. Xie, W. Ling, Y. Yuan, X. J. Lv, J. Lu, X. P. Hu, G. Zhao, and S. N. Zhu, "Efficiency-enhanced optical parametric down conversion for mid-infrared generation on a tandem periodically poled

MgO-doped stoichiometric lithium tantalate chip," Opt. Express **19**, 17500–17505 (2011).
14. T. Chen, B. Wu, P. Jiang, D. Yang, and Y. Shen, "High power efficient 3.81 μm emission from a fiber laser pumped aperiodically poled cascaded lithium niobate," IEEE Photon. Technol. Lett. **25**, 2000–2002 (2013).
15. Y. H. Liu, X. J. Lv, Z. D. Xie, X. P. Hu, Y. Yuan, J. Lu, L. N. Zhao, and S. N. Zhu, "Amplification assisted optical parametric oscillator in the mid-infrared region," Appl. Phys. B **106**, 267–270 (2012).
16. S. Sharabi, G. Porat, and A. Arie, "Improved idler beam quality via simultaneous parametric oscillation and signal-to-idler conversion," Opt. Lett. **39**, 2152–2155 (2014).
17. Z. G. Figen, O. Aytür, and O. Arıkan, "Idler-efficiency-enhanced long-wave infrared beam generation using aperiodic orientation-patterned GaAs gratings," Appl. Opt. **55**, 2404–2412 (2016).
18. O. P. Naraniya, M. R. Shenoy, and K. Thyagarajan, "Efficient scheme for mid-infrared generation using simultaneous optical parametric oscillators and DFG processes in a double-pass pump configuration," Appl. Opt. **54**, 7234–7239 (2015).
19. S. Li, P. Ju, Y. Liu, X. Jiang, R. Ni, G. Zhao, X. Lv, and S. Zhu, "Efficiency-enhanced picosecond mid-infrared optical parametric downconversion based on a cascaded optical superlattice," Chin. Opt. Lett. **14**, 041402 (2016).
20. A. Godard, M. Raybaut, T. Schmid, M. Lefebvre, A.-M. Michel, and M. Péalat, "Management of thermal effects in high-repetition-rate pulsed optical parametric oscillators," Opt. Lett. **35**, 3667–3669 (2010).
21. J. W. Haus, A. Pandey, and P. E. Powers, "Boosting quantum efficiency using multi-stage parametric amplification," Opt. Commun. **269**, 378–384 (2007).
22. Z. G. Figen, "Seeded optical parametric generator with efficiency-enhanced mid-wave infrared beam output," J. Mod. Opt. **61**, 1269–1281 (2014).
23. A. Godard, M. Raybaut, M. Lefebvre, A. M. Michel, and M. Péalat, "Tunable mid-infrared optical parametric oscillator with intracavity parametric amplification based on a dual-grating PPLN crystal," Appl. Phys. B **109**, 567–571 (2012).
24. T. Chen, H. Liu, W. Kong, and R. Shu, "Optimization of the tunable nanosecond cascaded optical parametric oscillators based on monolithic tandem lithium niobate superlattices," IEEE Photon. J. **8**, 1400209 (2016).
25. Y. Shen, S. Alam, K. K. Chen, D. Lin, S. Cai, B. Wu, P. Jiang, A. Malinowski, and D. J. Richardson, "PPMgLN-based high-power optical parametric oscillator pumped by Yb^{3+}-doped fiber amplifier incorporates active pulse shaping," IEEE J. Sel. Top. Quantum Electron. **15**, 385–392 (2009).
26. L. Zhang, H. Jiang, X. Yang, W. Pan, S. Cui, and Y. Feng, "Nearly-octave continuously wavelength tuning of a fiber laser," in *Lasers Congress 2016 (Advanced Solid State Lasers, Applications of Lasers for Sensing and Free Space Communications, Laser Applications Conference)*, OSA Technical Digest (Optical Society of America, 2016), paper ATh5A.6.
27. D. Lin, S. U. Alam, A. Malinowski, K. K. Chen, J. R. Hayes, J. C. Flannagan, V. Geddes, J. Nilsson, S. Ingram, S. Norman, and D. J. Richardson, "Temporally and spatially shaped fully-fiberized ytterbium-doped pulsed MOPA," Laser Phys. Lett. **8**, 747–753 (2011).
28. C. Drag, I. Ribet, M. Jeandron, M. Lefebvre, and E. Rosencher, "Temporal behavior of a high repetition rate infrared optical parametric oscillator based on periodically poled materials," Appl. Phys. B **73**, 195–200 (2001).
29. O. Gayer, Z. Sacks, E. Galun, and A. Arie, "Temperature and wavelength dependent refractive index equations for MgO-doped congruent and stoichiometric $LiNbO_3$," Appl. Phys. B **91**, 343–348 (2008).